Simulations of Primary Beam Sidelobe Confusion with the ATA Primary Beam

G. R. Harp, and M. C. H. Wright

March, 2007

Abstract

Wide angle measurements of the ATA primary beam pattern permit realistic simulations of the effects of far out sidelobes on image fidelity and dynamic range. We simulate continuum observations with the Allen Telescope Array using the results of the NRAO VLA Sky Survey. These simulations are weighted by the true ATA beam pattern and with a "perfect" Gaussian primary beam. When the true beam pattern is known, it is possible to deconvolve it from observations, but over most of the sky this will not be the case. Provided that we perform adaptive sidelobe calibration followed by peeling of the strongest sources (Sun, Cas A, Cyg A, etc.), we estimate a maximum dynamic range from 10^3 (ATA42) to 10^4 (ATA350) in continuum snapshots. For optimized earth rotation synthesis observations, confusion levels may be another factor of 5x smaller. The ATA is a pathfinder for the square kilometer array (SKA), and we extend these simulations to consider "stations" and their beam patterns currently proposed in the Large N Small D white paper of the US SKA consortium. We estimate phase errors in formation of the station beam introduce sidelobe confusion levels of 0.01%.

Introduction

Radio frequency interference (RFI) in radio astronomy is usually associated with man made signals generated by radio transmitters on earth or in orbiting satellites. But there are a handful of extremely bright, natural sources in the centimeter wavelength range (sun, Cassiopeia A, Cygnus A, etc.) which can be even more problematic in continuum observations, partly because they are noise-like and indistinguishable from the continuum sources under investigation. For example, at 1.4 GHz Cas A has a continuum flux of 1800 Jy, and this flux enters our radio telescope any time that Cas A is above the horizon. A typical far out sidelobe of the ATA primary dish might be -35 dB relative to the main beam at 1.4 GHz (Fig. 1), but even so it presents 177 mJy to our receivers. Interferometry reduces this confusion noise by a factor of N_{ant}. Even so, we expect that adaptive far sidelobe calibration (also known as peeling, ModCal, direction dependant self-cal) will be necessary to remove artifacts from strong sources if the ATA is to achieve its dynamic range goals for continuum imaging ($> 10^4$ for ATA 350).

Continuum sources generally have decreasing flux with increasing frequency. At some point, our calibration is limited by the sensitivity of our receivers and our ability to distinguish foreground sources from a smooth backround of unresolved sources. The latter point is addressed in (Bower 2000). We do not address these issues, the present memo assumes fluxes are high enough to get "good" (1%) calibrations at all frequencies.
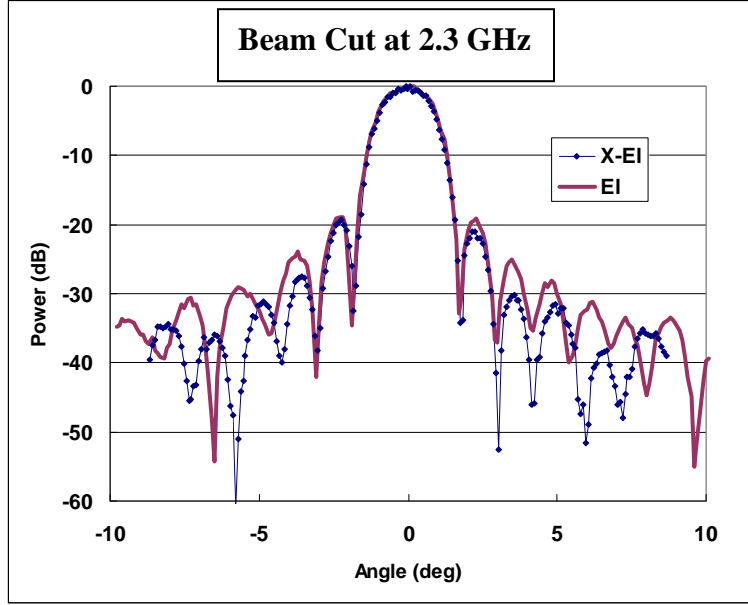
Figure 1: Two cuts through the primary beam pattern of one of the ATA dishes.

It has been argued that all ATA dishes are perfect to a small fraction of one wavelength, hence their sidelobe patterns must be identical. This greatly reduces the number of free parameters that must be determined for adaptive calibration or peeling. Recent measurements of the ATA primary beam pattern at 4 GHz (Fig. 2) indicate that antenna to antenna reproducibility is quite good. When we calculate the difference of the voltage patterns in Fig. 2, we observe 4% RMS voltage variation over 400 square degrees (533 square beam widths). Unfortunately, this is not sufficient reproducibility to eliminate the need for peeling of strong sources.

The elliptical beam shape in Fig. 2 is a reflection of the polarization asymmetry of the ATA primary beam pattern. The offset Gregorian antenna is designed to have zero polarization squint and equal polarization gain along boresight. However, this property cannot be preserved off boresight. As it happens, the geostationary satellite used for the measurements in Fig. 2 has a strong linear polarization. This fortuitous example demonstrates an important point: when the sky contains polarized sources, the polarization corrupts attempts to measure total power (stokes parameter I) unless the beam pattern polarization is explicitly characterized and removed. This is evident from the expressions for the XX and YY cross correlations in terms of Stoke's parameters:

$$XX = I + Q \cos(2\chi) + U \sin(2\chi)$$

$$YY = I - Q \sin(2\chi) + U \cos(2\chi)$$

where χ is the parallactic angle. In this case, the satellite contains strong Q and U terms. The co-polarized XX and YY beam patterns are known to be elliptical in shape with major and minor axes aligned with the vertical and horizontal. This is also true for the cross-polarized XY and YX patterns which have a different shape. All this variation leads to the diagonally aligned elliptical shapes in the measured patterns.

2

This result was anticipated in a recent SKA memo (Thompson 2003) where Thompson argues that for any dish of substantial size, the sidelobe levels at large angles the main beam result "mainly from scattering from feed supports, surface errors, feed spillover and similar unwanted effects which are larger than the $J_1(x)/x$ oscillations resulting from the diffraction at the circular aperture. [Therefore] it is likely that the detailed structure of the far sidelobes differs from one nominally-identical antenna to another."
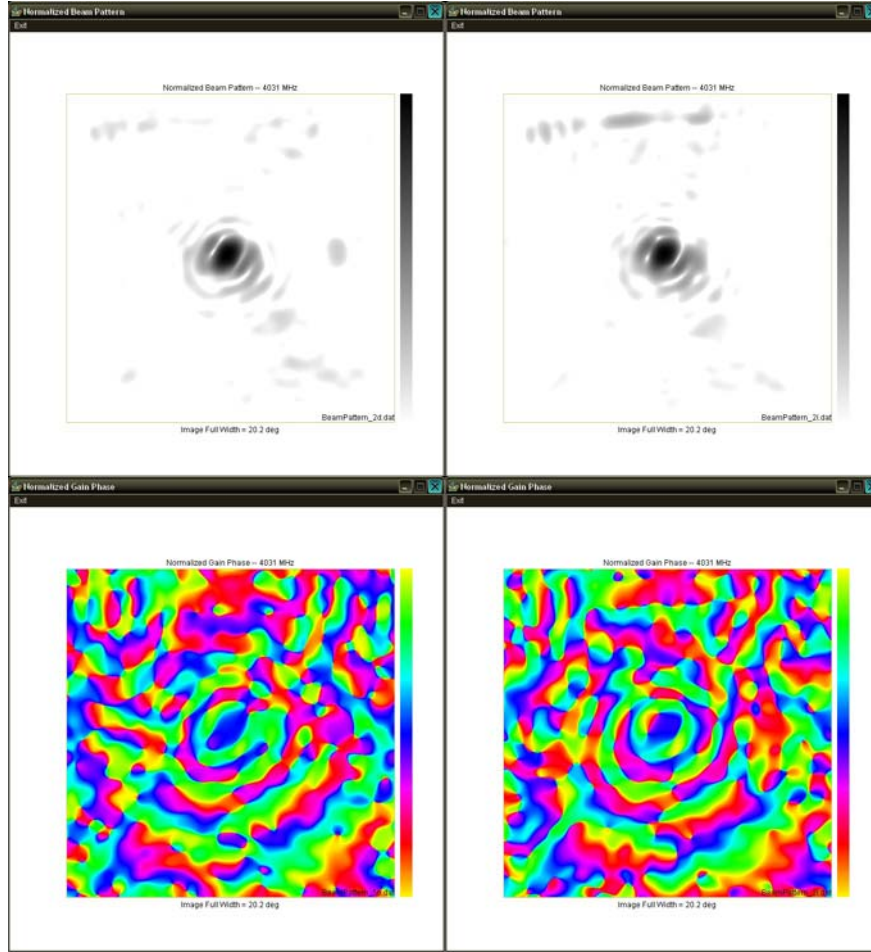

Figure 2: Primary beam power patterns (top) and phase (bottom) for two ATA dishes measured at 4 GHz on a linearly polarized geostationary satellite. The satellite polarization causes the elliptical shape of the main lobe; the circularly polarized pattern (hence unpolarized pattern) is more circular (see Fig. 5 for one example).

Another argument says that we can simply measure the beam patterns of all antennas and be done with it. Whilst the patterns are known to be stable on a timescale of at least a week, a straightforward calculation shows this is not possible. Nyquist sampling of the complete primary beam pattern requires about

$$N = \frac{2\pi R^2}{\lambda^2}$$

pointings. R is not necessarily the radius of the dish, but rather the longest path length of any signal that scatters into the receiver. For the ATA dish (radius 3 m), path lengths for waves scattered from support structures may be as large as 12 m. With increasing frequency, the pattern must be re-measured each time R/l changes by ~1. To fully measure one ATA primary beam pattern over 1-10 GHz frequency range would require 2 x 10^{10} pointings (Fig. 3), or 600 years at one second per pointing! The situation becomes worse for larger dishes.[†]

In this memo, we consider how errors in the primary beam sidelobe pattern will affect continuum confusion levels at the ATA in the absence of peeling. To do this we perform simulations based upon the NRAO VLA Sky Survey (NVSS) (J. J. Condon 1998). According to the NVSS website, "This radio survey used the NRAO Very Large Array telescope and covers the sky north of a declination of -40 degrees at a frequency of 1.4 GHz, a resolution of 45" and a limiting peak source brightness of about 2.5 mJy/beam." By weighting NVSS results with ATA primary beam pattern measurements, we obtain reliable simulations of what the ATA may measure. Comparing these with other simulations assuming a "perfect" Gaussian primary beam, we estimate sidelobe confusion.

We follow these results with a second set of simulations using the "primary" beam pattern of a phased 15 element array of antennas. We consider the effects of corrupting phase noise in the array beam. When the beamforming is imperfectly controlled, sidelobe confusion is unavoidable.
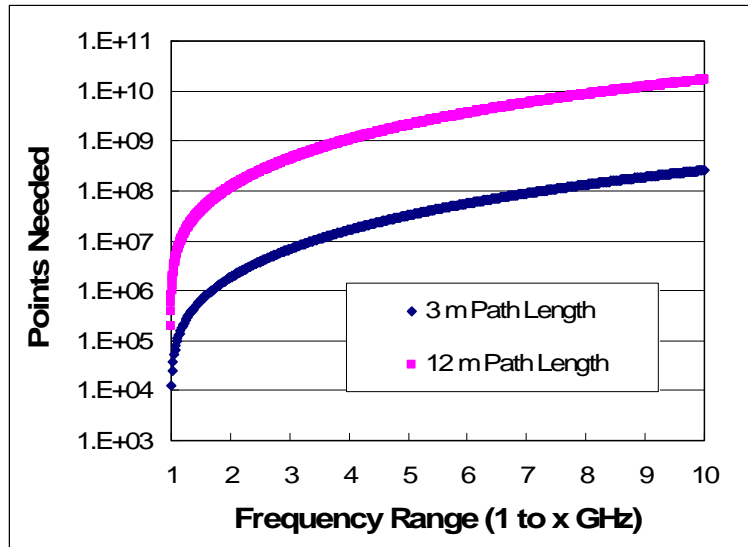

Figure 3: Estimate of the number of pointings required to measure ATA primary beam pattern as a function of frequency range.

[†] For single-frequency surveys, it is not necessary to measure the beam pattern at all frequencies. For example, a single frequency at 5 GHz requires ~250,000 pointings which could be accomplished in a few days. As we see below, the worst sidelobes are within ~10 degrees of boresight. If only this limited region of the beam pattern is measured, it can be done in ~1000 pointings. This is more promising; provided the beam pattern is reproducible over time periods much greater than the time to acquire the data.

Simulations

Figure 4 presents the entire celestial sphere at 1.4 GHz in Mercator projection as measured in NVSS. The color scale spans 60 dB in flux, where the brightest source is Cas A. The simulation was calculated by taking all of the nearly 2 million NVSS component sources and binning them into the 1024 x 512 pixels of the image. The nature of the Mercator projection gives lower source density at the poles, which explains the reduced brightness at the top of the image. The black stripe at image bottom is the area of the sky not measured by NVSS. Mercator is chosen as a convenient projection for display, but in the simulations below the computer works in terms of "true" angles so this does not influence the results.
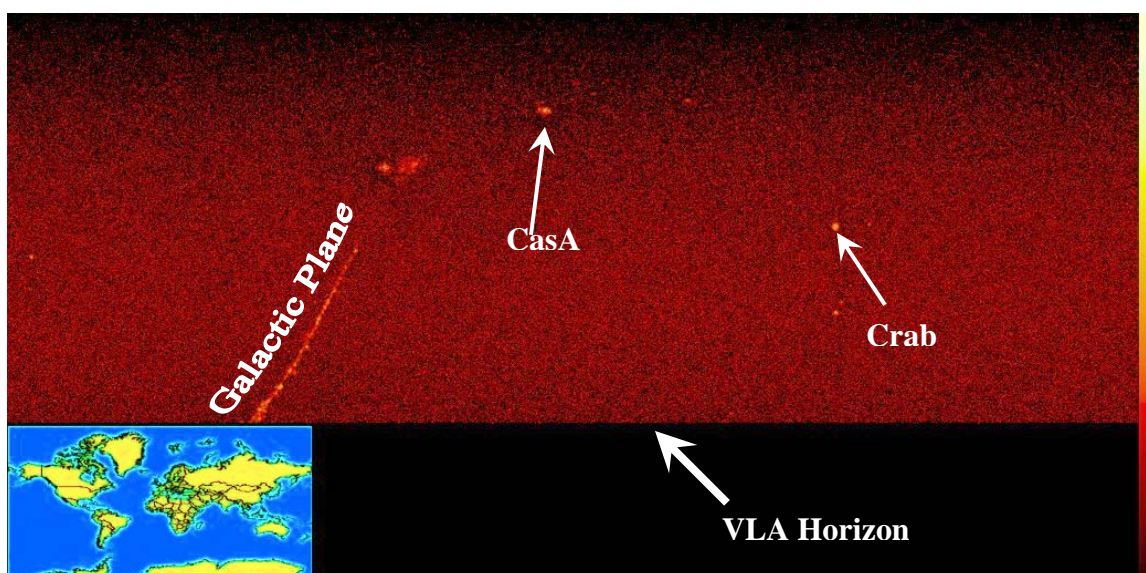

Figure 4: Entire sky in Mercator projection as observed by the NVSS Survey. At image center is the point (RA, Dec) = (0 hr, 0°). The left and right edges correspond to RA = ±12 hr. Top is the north celestial pole and bottom is south pole. Color intensity is on a log scale, with CasA at 0 dB and spanning 60 dB in power. INSET: Mercator projection of world map for comparison.

The ATA primary beam pattern (Fig. 5) was measured over the entire accessible sky using the circularly-polarized, geostationary satellite XM-2 as a bright, point source (Harp 2004). The complex beam pattern was collected using a cross correlation technique, where one antenna is pointed directly at the satellite (reference antenna) and a second antenna is swept over all possible azimuths and elevations. These data are reprojected onto the beam pattern sphere (non-trivial projection because the parallactic angle changes with pointing). The data collection and reduction are described in detail in (Harp 2004).
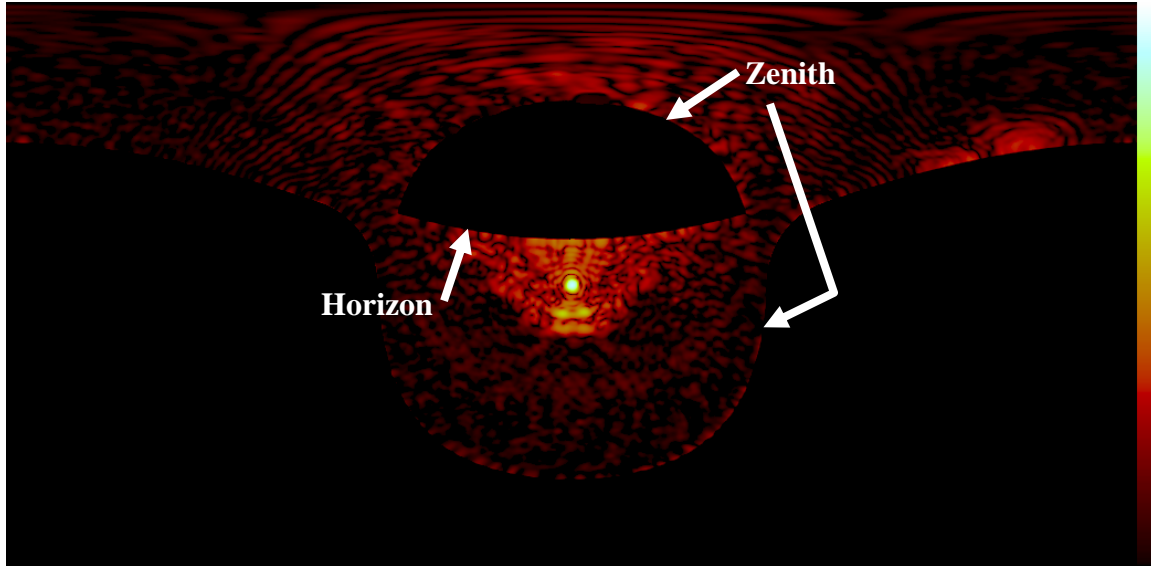
Figure 5: Primary beam power pattern as measured at the ATA. Projection is the same as previous figure with antenna pointed at (RA, Dec) = (0, 0). Logarithmic intensity scale is 0 to -50 dB relative to the beam maximum – note different scale than Fig. 4). The black regions correspond to areas that could not be measured due to pointing geometry.

At the center of Fig. 5 we see the primary beam pattern at 2.3. GHz. Measurable sidelobes are observed over most of the sky, even when the dish is pointed more than 90° away from the satellite source. This pattern of a single antenna is reproducible at a level below -40 dB in measurements separated by a week (Harp 2004). Beyond the first sidelobe ring, the strongest sidelobe features appear at 1-2% power level about 10° below the main beam in Fig. 5. These "dog's sunglasses" probably arise from scattering from the shroud – an aluminum shield placed around the feed to shield it from ground radiation. This shroud is not a precision machined form, hence the dog's sunglasses is expected to vary in amplitude from dish to dish. (To see the face of the dog, turn the image upside down.)

Notice that the ATA beam pattern was measured at 2.3 GHz while the NVSS survey was measured at 1.4 GHz. This inconsistency can be resolved by supposing that the continuum intensity of the sky is the same at 2.3 GHz as at 1.4 GHz, apart from an overall scaling factor. Another view is to suppose that the primary beam pattern is equivalent to the pattern of an otherwise identical 10 m dish at 1.4 GHz. Because we are concerned only with relative comparisons, either of these assumptions are not much of an imposition on the results.

Results

Fig. 6 panel A focuses on the central 22.5° x 22.5° area of Fig. 4. At this magnification the pixelization of the simulation begins to appear; the pixels are 0.35° square. By comparison, the primary beam pattern FWHM is 1.5° at 2.3 GHz, and its central maximum spans ~20 pixels. Consequently, these simulations give a representative estimate of source intensity but not high image fidelity. This poses no problem for the conclusions of this paper.
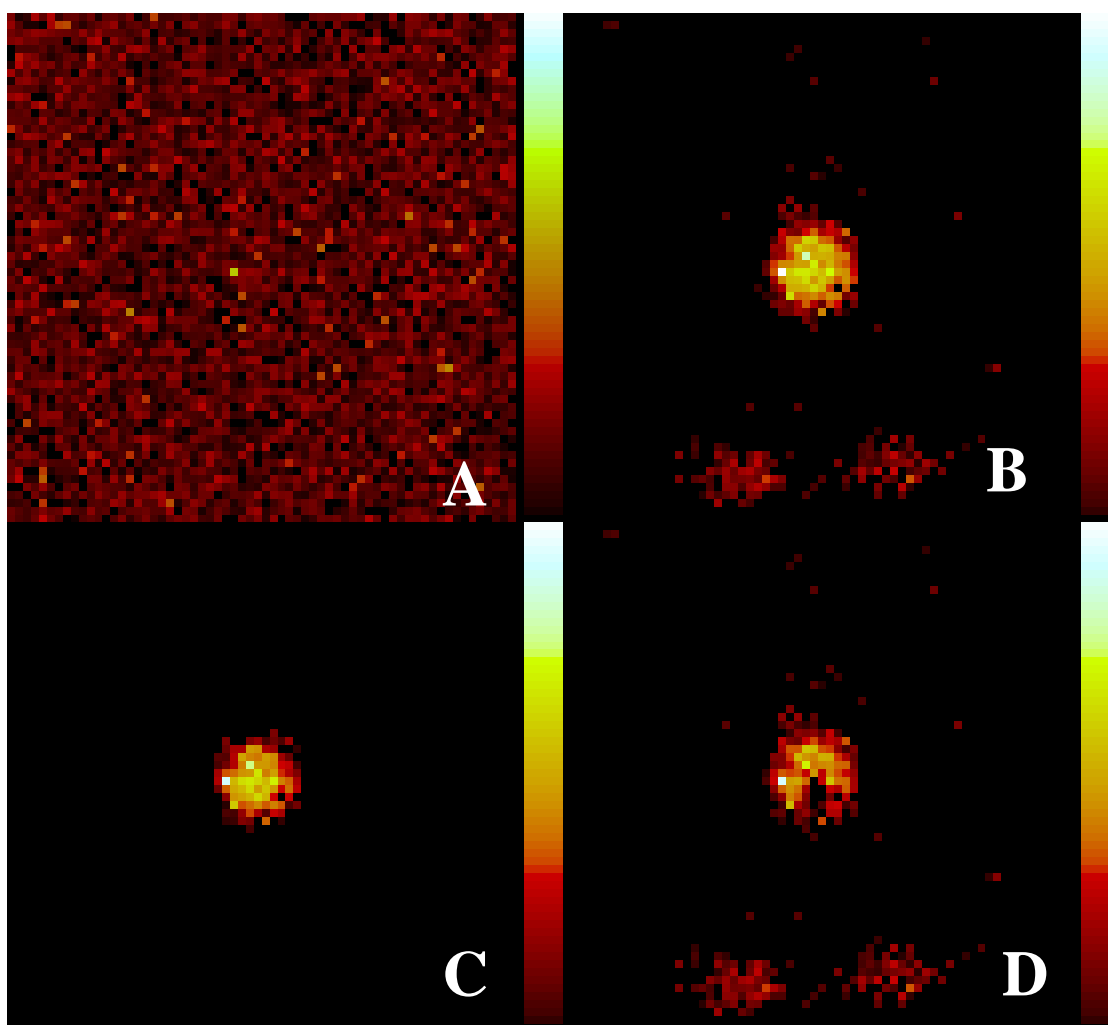
Figure 6: Simulations of a small area (22.5° x 22.5°) of the sky centered on (RA, Dec) = (0,0). (A) the original NVSS Survey results binned into 0.35° x 0.35° pixels. The original intensity scale puts Cas A at 0 dB (white) and any pixel below -60 dB as black. Note: Cas A does not appear in this image. (B) Similar to panel A, but multiplied by the measured ATA primary beam pattern. To bring out detail, this image spans only 40 dB where the brightest pixel is taken as the reference level. (C) Similar to panel B, but NVSS has been multiplied by Gaussian beam pattern. Intensity scale is identical to panel B. (D) The difference of panels B and C, intensity scale same.

To get a feeling of how the primary beam will vignette the image, we form the product of Figs. 4 and 5, shown in panel B. The central maximum of the primary beam is clearly evident, as are the dog's sunglasses. Closer inspection reveals ~20 bright point sources far from either of these features, 30 dB weaker than image center. None of these sources appear in panel C, where we substitute the ATA beam with a Gaussian beam pattern. The Gaussian was chosen to have the same FWHM as the ATA beam. Finally, panel D shows the difference image. Notice that all color scales are logarithmic, with panel A spanning 60 dB relative to Cas A, while panels B, C, and D span 40 dB relative to the brightest pixel in panel B.

Radial offset	Beam flux	Gaus flux	Flux Difference
Beam widths	mJy	mJy	mJy
0.05	3.6	3.6	0
0.05	12.1	12.1	0
0.11	3.7	3.7	0
0.12	5.7	5.7	0
0.12	2.6	2.6	0
0.15	3.2	2.7	0.5
0.16	2.7	2.5	0.2
0.17	2.5	2.3	0.2
0.17	4.8	4.1	0.7
0.20	1.8	1.8	0
0.22	3.7	3.4	0.3
0.22	7.2	6.8	0.4
0.23	10.2	8.8	1.4
0.23	3.8	3.5	0.3
0.24	2.8	2.1	0.7
0.25	210.4	182.5	27.9
0.25	8.4	7.3	1.1
0.25	2.3	2.1	0.2
0.25	6.6	6.6	0
0.25	5.1	4.3	0.8
0.25	10.9	10.9	0
0.25	3.3	3.1	0.2

Table 1: Listing of the point sources within 0.25 beam widths of the primary beam in Fig. 6. The first column shows the radial distance from beam center, the second and third columns show the beam weighted flux and Gaussian weighted flux, respectively. The last column displays their difference.

A more quantitative comparison is made in Table 1. Here we list the NVSS sources in the vicinity of the primary beam peak, showing their fluxes after weighting by either the measured ATA beam or by the Gaussian approximation. Very close to beam center the two fluxes are identical, but small amplitude discrepancies between ATA beam and Gaussian beam result in ~10% flux differences only 0.25 beam widths away from the pointing center.

For sources this close to beam center, we expect that it will be possible to calibrate the primary beam pattern and deconvolve it from the image. But at great distances from beam center only adaptive peeling can be used.

The same data are plotted on a wider scale in Fig. 7. Here we have collapsed the beam weighted flux into bins of near equal radius from the pointing center. That is, we take all the sources in an annulus that is one beam width wide and centered at an integral number of beam widths from center. In Fig. 7 the beam flux for annuli near the center are quite similar for ATA beam weighting and Gaussian beam weighting. But the Gaussian weighted flux tends rapidly to zero with increasing distance from beam center. The ATA beam weighted flux does not tend to zero, but hovers in the range of a few mJy per annulus with increasing distance. Notice the "dog's sunglasses" appear in this plot at 6.5 beam widths = 10°.
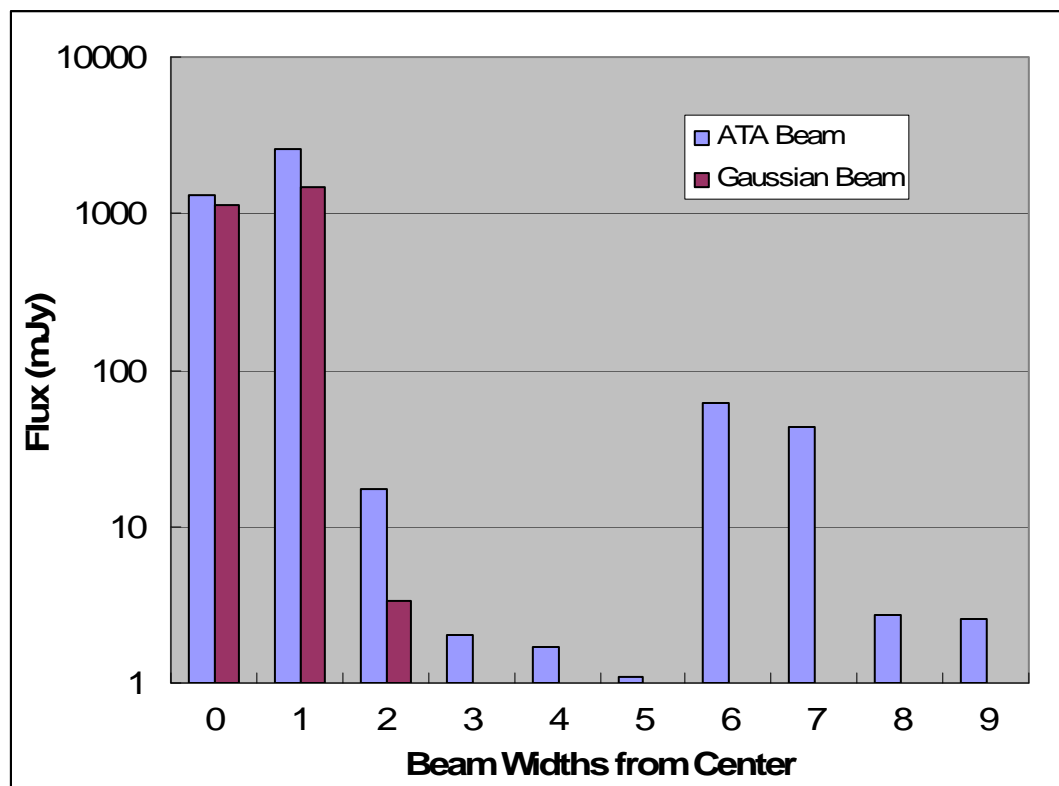

Figure 7: Comparison of the NVSS flux observed in annuli at various distances from primary beam center. The NVSS sources are first weighted with either the measured ATA beam or with a Gaussian beam, and the source flux is then integrated over an annulus that is 1 primary beam width wide. The two beam patterns are normalized to be identical on boresight. The radial distance of the annulus from beam center is displayed on the horizontal axis and integrated, weighted flux on the vertical axis.

As a concrete example, let suppose that we perform a snapshot observation, and that we have accurate knowledge of the ATA beam pattern over an angular range of +/- 2 beam widths (10° diameter at 1.4 GHz). We can correct images near the primary center, but the flux from 3-9 beam widths on the graph above will appear as confusion in the image. The confusing flux in this example is **3%**.
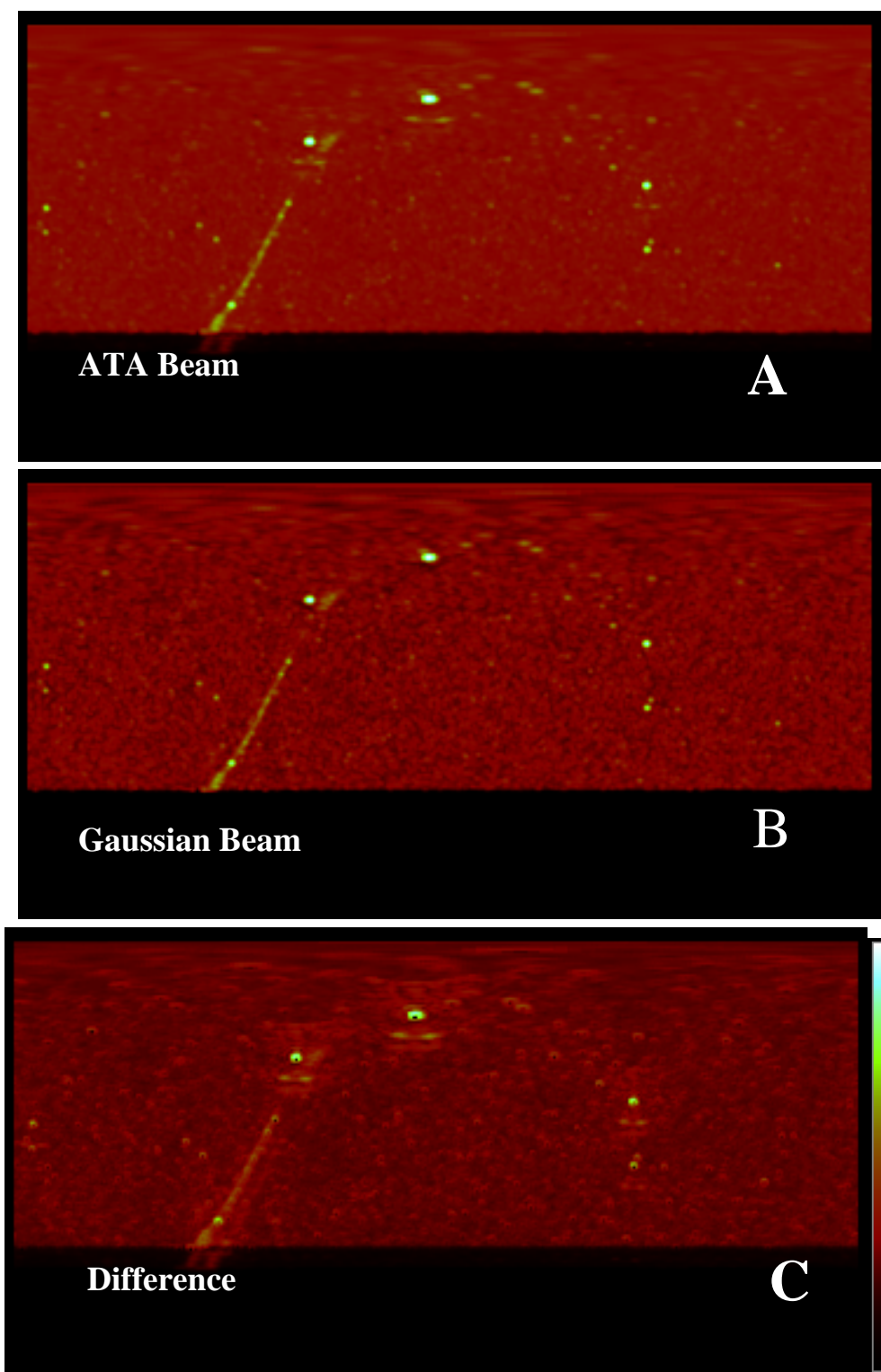
Figure 8: Simulations of the NVSS survey convolved with (A) the ATA primary beam and (B) a Gaussian primary beam pattern. Panel (C) shows the difference image. The color scale in panel C is appropriate for all images and spans 40 dB.

These calculations begin to describe the differences we can expect between the ATA beam and a Gaussian beam. These differences are of the same order of magnitude as the difference between the primary beams on 2 different ATA dishes (c.f. Fig. 2). As a last comparison of this kind, we simulate single-dish observations of the entire sky using the ATA beam and Gaussian beam. The results of these simulations are shown in Fig. 8.

One striking difference between the beams is the reduced dynamic range in the ATA result. The far sidelobe pattern of the ATA beam spreads confusing flux evenly throughout the image. It is a good thing if this flux is spread evenly; it might be possible to estimate it as a constant value and subtract it off. Even better, interferometric measurements will be insensitive to this constant offset.

Unfortunately, the confusing flux is not perfectly smooth. Below each bright source in Fig. 8 we observe an image of the dog's sunglasses. Such confusing features are even more evident in Fig. 8, C (difference image). We conclude that interferometric measurements will be corrupted by non-zero spatial frequencies in Fig. 8 C. The dog's sunglasses will appear especially in short baselines whereas isolated bright point sources (c.f. Fig. 6D) will show up in long baselines.

Remarks on ATA Primary Beam Simulations

Returning to the 3% confusion level of Fig. 7, notice that this result does NOT change when scatterers are placed in the ATA shroud (as is planned). These scatterers disperse the dog's sunglasses more evenly across the sky and this is generally good. However, at this angular scale the sky has fairly uniform brightness, so the integrated confusion level is about the same.

The 3% level will be reduced when averaged across many antennas, assuming their sidelobes are not identical. For incoherent sidelobe averaging, we expect a reduction by N. For ATA 42 or 350 we calculate confusion levels of 0.1% or 0.01%, respectively.

An additional reduction is expected in observations using earth rotation synthesis, because the parallactic angle rotates as the source moves across the sky. Following Fig. 7, we choose a median radius of 7 beam widths from the center for strong sidelobes. Over a horizon to horizon observation, the parallactic angle changes my ~180°, giving roughly 21 independent projections of the sidelobe pattern. Again the sidelobes average as N, in this case N is the number of projections. We conclude that earth rotation synthesis is likely to reduce confusion levels by another factor of 13 dB.

Station Beams

The next generation large radio telescope is known as the square kilometer array, and is presently in the concept / preliminary design stages. The ATA is a model for the SKA, as it delivers a large collecting area over a wide frequency range at modest cost. In one design for the SKA, the US SKA consortium proposed the use of "station" beamforming to reduce processing costs in the large number of small diameter (LNSD) dishes. In station beamforming, the dishes are clustered together in groups of ~15 elements, and synthetic beamforming is performed with the signals from each group. These "station"

beams are then cross correlated to form images, rather than cross correlating every antenna element, which reduces the number of correlations by a factor of $\sim15^2$. According to the US SKA consortium (US-SKA 2002), "Our best current estimate is that 160 stations between 35 km and 3500 km, each with 13 antennas will be adequate to achieve the design goals of the SKA, taking into account the beneficial effects of multifrequency synthesis." Note that the ATA does not use station beams.

Whether or not station beams give good value for money is still an unresolved question because the effects of station beamforming on image fidelity are not well understood. For example, if the station beams are perfectly calibrated then the beam shape may be deconvolved from images using conventional techniques. But our knowledge of element gains and phases is usually imperfect, and because calibration information is lost in the beamforming process, station beamforming inevitably degrades the resultant image.

As a contribution to the discussion surrounding station beams, we present simulations of sidelobe confusion that appears when station beams are slightly imperfect. To simulate a primary beam response for an SKA station, we made a snapshot beam for an optimized CARMA compact configuration of 15 antennas scaled to 1.4 GHz.. The RMS sidelobe response is $7\% = (N_{sta})^{-1}$, where N_{sta} is the number of antennas per station. The resulting beam pattern is displayed in Fig. 9. The image has a logarithmic intensity scale spanning 40 dB.
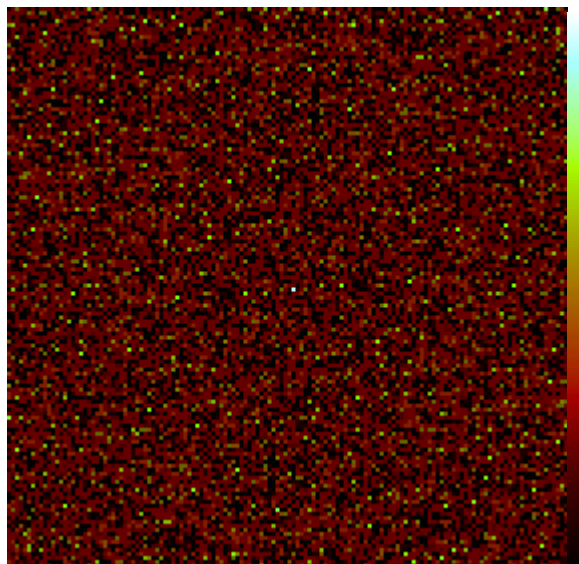

Figure 9: 49° x 49° patch of the synthetic beam pattern of a 15 element array. Dynamic range is 40 dB The main beam appears in only the center pixel and is white with a value of 0 dB, with all other pixels being weaker.

The main lobe of this beam occupies only one pixel at the center. With 1° sampling, these images undersample the beam pattern, but each pixel represents a fair sample in the sense that it is representative of true level of the beam pattern at the center of each pixel. Notice

that in this sample there are no strong sidelobes within a few degrees of the main lobe, which is a reflection of the optimization of antenna positions.

The actual primary beam response for a phased array station beam depends on the amplitude and phase of the wavefront at each antenna in the station and will suffer from errors in the estimated atmospheric phase, which is dominated by the troposphere at high frequencies and ionosphere at low frequencies. To simulate the error pattern we applied random, 1 degree RMS phase errors to each antenna in the phased beam. The error pattern is visually indistinguishable from Fig. 9, but has an RMS difference with the original beam pattern of 0.36% with peak errors of ± 1.3%.

We repeat the processing of Fig. 8 using the perfect and error station beam patterns. We first form the product of the synthetic beam pattern with the ATA primary beam pattern because stations will, of course, be comprised of parabolic dishes like those at the ATA. For the purposes of discussion we shall suppose that the ATA beam pattern in this case represents that of a 10 m dish at 1.4 GHz.
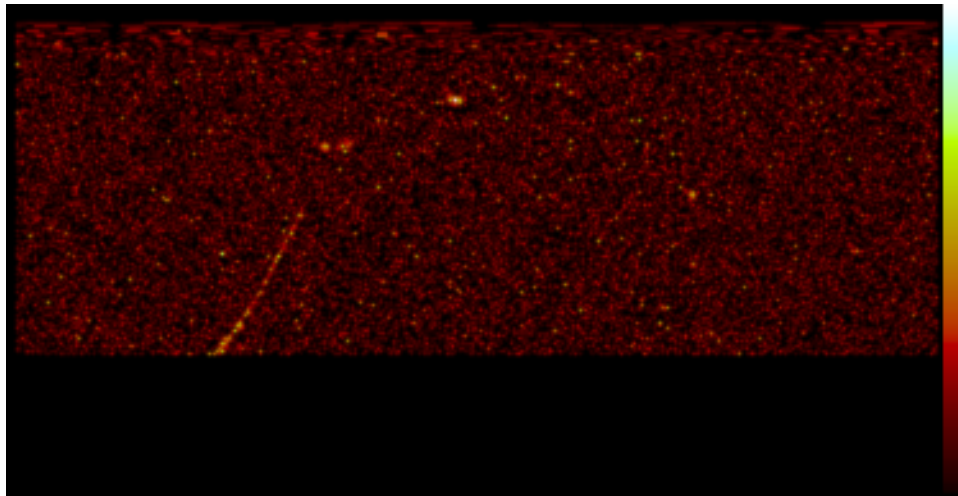

Figure 10: Convolution of the NVSS survey with the perfect station beam pattern. The station beam is formed by multiplying Fig. 9 by the primary beam pattern of a 10 meter dish. The color scale is logarithmic and spans 40 dB with Cas A at 0 dB.

Figure 10 displays the convolution of the perfect station beam with the NVSS survey. It looks very similar to Fig. 4 partly because the station beam is only 1 pixel wide. By deconvolving the known perfect beam pattern, presumably we could recover Fig. 4 with high accuracy. The convolution of NVSS with the error beam pattern is visually indistinguishable from Fig. 10. To bring out the changes, we form the difference of Fig. 10 with the error beam convolution, and plot it in Fig. 11.
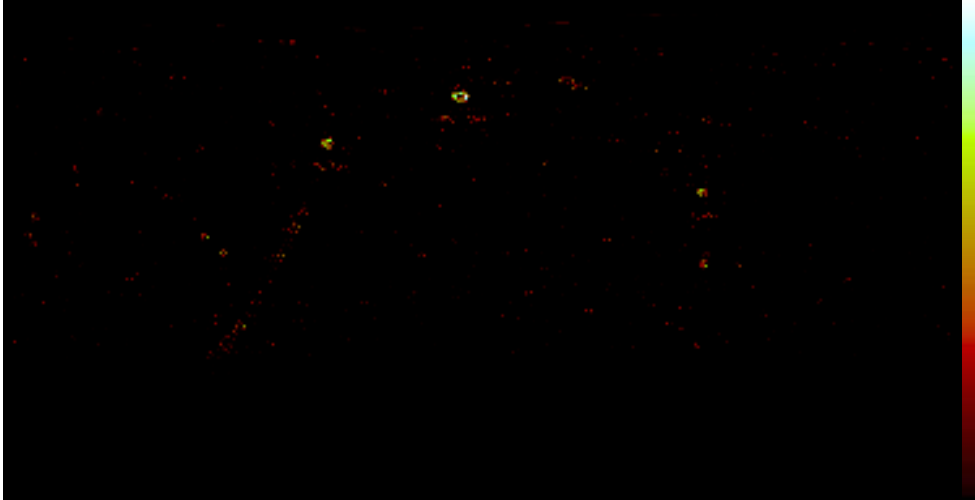
Figure 11: Difference between the perfect station beam and error station beam convolutions. The color scale is logarithmic and spans -40 to -80 dB in intensity, relative to Fig. 10. That is, the brightest feature in this image is ~40 dB weaker than the brightest feature in Fig. 10.

The primary beam pattern apodizes the station beam, and the convolution tends to smooth strong variations between the perfect and error beams. Hence the strongest difference observed in Fig. 11 is ~40 dB weaker than the strongest feature in Fig. 10. Not surprisingly, the strongest difference appears in the vicinity of Cas A. There is strong visual correlation between Figs. 10 and 11, indicating that the confusion levels in the station beam are strongly correlated with the intensity levels in the vicinity of the original image, but reduced by a factor of 10,000.

Remarks on Station Beam Simulations

If the SKA can achieve 40 dB confusion levels in a station beam snapshot, then this is not a limiting factor for SKA design. Given that this confusion is mitigated by 1) variations from station to station, 2) earth rotation synthesis, and 3) adaptive peeling, it should be possible to meet the SKA goals of 10^6 dynamic range in total power.

Discussion

ATA

These simulations are encouraging. At the ATA, there are large areas of the sky, mostly out of the galactic plane, where sidelobe confusion levels represent 0.1% (ATA42) or 0.01% (ATA350), implying a dynamic range of 10^3 to 10^4, respectively. This is true, however, only at night and only when no other strong sources are up, such as Cas A, Cyg A, Tau A, etc. (the "A" team, after Jan Noordham). In our first measurements at the ATA we have already seen how Sun in sidelobes makes imaging almost impossible.

Fortunately we have adaptive peeling. In this method, we self-calibrate on extremely bright sources in the sidelobes and subtract the source directly from the UV data. This calibration must be adaptive and is generally quite different from calibration for the field of view due to the complex antenna primary beam patterns described here. Far from the main lobe, every antenna has a unique complex voltage pattern. This introduces time

dependant amplitude and phase (i.e. polarization) fluctuations in each baseline. Since it is impossible to calibrate the beam patterns in advance, we must do it on the fly. Routines for peeling are already in wide use (e.g. ModCal in DRAO Northern Sky Survey software, UVCal and other routines in MIRIAD). Note that even if it were possible to precalibrate the beam patterns, ionospheric fluctuations (at low frequency) and tropospheric fluctuations (at high frequency) insert a complicated phase screen between the array and the sky. This phase screen frustrates our hope to avoid peeling over much of the ATA frequency range.

Successful peeling requires that correlations be stored with little frequency and time averaging (T.J. Cornwell 2004). The integration time must be shorter than the timescale of variation of the RFI signal on each baseline, or the amplitudes will not close (i.e. no antenna-based gain calibration is possible) (R. Perley 2003). Reducing the frequency channel width permits longer time averaging without loss of data, so frequency averaging and time averaging trade off in the usual way.

As with any other RFI mitigation, our ability to self-cal and peel is limited by signal to noise. Considering the simulation of Fig. 7, we can expect ~ 2 Jy flux in a typical dark field. Peeling must be done in snapshot mode, since primary beam rotates rapidly with parallactic angle. The dynamic range (10^3 or 10^4) factor is approximately cancelled by the primary beam dynamic range ($10^3 - 10^4$ between main lobe and far sidelobe). We must achieve substantial SNR to self calibrate (e.g. 10), hence we cannot peel any source weaker than ~ 20 Jy (there are 300,000 sources with flux > 20 Jy in the NVSS Catalog). This also means that we cannot beat the dynamic range estimates presented here with peeling alone. Larger SNR expected for the SKA leads to proportionally smaller peeling limits.

When peeling, it is necessary to perform a joint self calibration with the two antenna polarizations. The elliptical shape of the beam pattern in Fig. 2 demonstrates how total power I is mixed with polarized power Q, U, and V by complex sidelobe structure. This is especially true for polarized observations, where, say, Q is corrupted by unpolarized radiation entering a polarized antenna sidelobe. But the converse is also true as total power observations can be corrupted when polarized radiation is "depolarized" as it enters the same sidelobe. Although the polarized radiation is usually one or two orders of magnitude smaller than the unpolarized component, this effect is not neglible even in total power observations.

Several new ideas are floating around the calibration community with regard to peeling and associated techniques. One is that primary beam pattern (and/or isoplanatic patch of atmosphere) varies slowly on the sky as compared to most point sources. Hence unconstrained peeling can simulate unphysical variations in beam pattern gain for two closely spaced sources. Especially at the SKA, it is necessary to constrain calibration variations to physical levels. This increases complexity but is generally good since it reduces the number of degrees of freedom in the gain solution. Also, if there are sufficient numbers of baselines then primary beam and atmospheric effects might be determined independently. It may be valuable to store the self-calibrated primary beam

pattern for future observations. This might useful in cases where we observe the same sources day after day.

SKA

As for station beams, one problem not considered here is what happens when an antenna fails. The station beam simulations use an optimized antenna configuration, but this optimization is not preserved when one antenna goes down (N_{ant} is small). This may pose a significant problem, as seen in Fig. 11. In the difference image between the perfectly and imperfectly calibrated beams we notice a "hole" centered on each bright source in the image. Here the beams agree despite the miscalibration, partly because the sidelobes near the center of the station beam are small. The sidelobes further out are attenuated by the primary beam, so we obtain good resistance to calibration errors. But if one antenna were to drop out close-in sidelobes are likely to appear and the station may become more sensitive to calibration errors. Further simulations are necessary to determine if this is the case.

Conclusions

These simulations of continuum confusion in the primary beam sidelobes provide quantitative estimates of the dynamic range that can be achieved with only minimal peeling. Broadly speaking, we find that confusion levels are acceptable. But our results show clearly that ATA must employ direction dependant self-calibration to peel the "A" team sources (Cas A, Cyg A, Tau A, Vir A, etc.) when they are above the horizon. This is doubly true for Sun. Although this idea is recently come to the ATA, it is already well appreciated in the calibration community.

One of the authors (MCHW) has already developed software to peel bright sources in collaboration with the Backer's group doing low frequency observations (150 MHz) at Green Bank. Similar developments are proceeding at several observatories around the world. If we are to continue improving the sensitivity and fidelity of our images in radio astronomy, we must focus our energies on improved calibration.

Bibliography

Bower, G. C. (2000). Confusion, Dynamic Range and Array Size for the ATA. ATA Memo Series. **9**.

Harp, G. R. (2004). Holography at the ATA. R. F. Ackermann. ATA Memo Series. **65**.

J. J. Condon, e. a. (1998). The NRAO VLA Sky Survey. Astrophysical Journal. **115:** 1693.

R. Perley, T. J. C. (2003). Removing RFI Through Astronomical Image Processing.

T.J. Cornwell, R. A. P., K. Golap, S. Bhatnagar (2004). RFI Excision in Synthesis Imaging Without a Reference Signal. EVLA Memo Series. **86**.

Thompson, A. R. (2003). Spatial Nulling for Attenuation of Interfering Signals. SKA Memo Series. **34**.

US-SKA, C. (2002). Square Kilometer Array Preliminary Strawman Design Large N - Small D. SKA Memo Series. **18**.